Available online at www.sciencedirect.com
ScienceDirect
Journal of Organometallic Chemistry 692 (2007) 3277–3290
Journal of Organometallic Chemistry
www.elsevier.com/locate/jorganchem

Spectroscopic properties and electronic structures of 17-electron half-sandwich ruthenium acetylide complexes, $[Ru(CCAr)(L_2)Cp']^+$ (Ar = phenyl, *p*-tolyl, 1-naphthyl, 9-anthryl; $L_2 = (PPh_3)_2$, $Cp' = Cp$; $L_2 = dppe$; $Cp' = Cp^*$)

Mark A. Fox [a], Rachel L. Roberts [a], Wan M. Khairul [a], František Hartl [b], Paul J. Low [a,*]

[a] *Department of Chemistry, Durham University, South Rd., Durham DH1 3LE, UK*
[b] *Van't Hoff Institute for Molecular Sciences, University of Amsterdam, Nieuwe Achtergracht 166, 1018 WV Amsterdam, The Netherlands*

Received 29 January 2007; received in revised form 26 March 2007; accepted 26 March 2007
Available online 5 April 2007

Abstract

A series of half-sandwich bis(phosphine) ruthenium acetylide complexes $[Ru(C{\equiv}CAr)(L_2)Cp']$ (Ar = phenyl, *p*-tolyl, 1-naphthyl, 9-anthryl; $L_2 = (PPh_3)_2$, $Cp' = Cp$; $L_2 = dppe$; $Cp' = Cp^*$) have been examined using electrochemical and spectroelectrochemical methods. One-electron oxidation of these complexes gave the corresponding radical cations $[Ru(C{\equiv}CAr)(L_2)Cp']^+$. Those cations based on $Ru(dppe)Cp^*$, or which feature a *para*-tolyl acetylide substituent, are more chemically robust than examples featuring the $Ru(PPh_3)_2Cp$ moiety, permitting good quality UV–Vis-NIR and IR spectroscopic data to be obtained using spectroelectrochemical methods. On the basis of TD DFT calculations, the low energy (NIR) absorption bands in the experimental electronic spectra for most of these radical cations are assigned to transitions between the β-HOSO and β-LUSO, both of which have appreciable metal d and ethynyl π character. However, the large contribution from the anthryl moiety to the frontier orbitals of $[Ru(C{\equiv}CC_{14}H_9)(L_2)Cp']^+$ suggests compounds containing this moiety should be described as metal-stabilised anthryl radical cations.
© 2007 Elsevier B.V. All rights reserved.

Keywords: Ruthenium; Acetylide; Radical cation; Spectroelectrochemistry; TD DFT

1. Introduction

Metal acetylide complexes have been objects of intense research activity for decades [1–7]. While much of the early work was naturally concerned with synthetic and structural issues, there is a considerable and growing body of contemporary interest concerning the electronic, optical, non-linear optical and magnetic properties of these compounds [8–11]. Comparisons of the properties of half-sandwich ruthenium acetylides $[Ru(C{\equiv}CR)(L_2)(\eta^5\text{-}C_5R_5)]$, where L_2 usually represents supporting phosphine ligands, with analogous iron complexes have been made, with the general conclusion being that iron gives rise to much greater metal character in the frontier orbitals, whilst the ruthenium analogues exhibit far greater Ru(d)–acetylide(π) mixing [12–16]. This greater delocalisation is also found to persist after one-electron oxidation of the ruthenium complexes, and has been used to rationalise the greater chemical reactivity of the 17-electron radical cations $[Ru(C{\equiv}C\text{-}1,4\text{-}C_6H_4X)(dppe)(\eta^5\text{-}C_5Me_5)]^+$ [13] when considered alongside the radical cations $[Fe(C{\equiv}CC_6H_4\text{-}X)(dppe)Cp^*]^+$ (X = CN, CF_3, Br, F, Me, ^{t}Bu, OMe, NH_2, NMe_2), which have been isolated as the $[PF_6]^-$ salts [16].

In this report we describe the cation radicals generated from the series $[Ru(C{\equiv}CAr)(L_2)Cp']$ [Ar = C_6H_5 (**1**), C_6H_4Me-4 (**2**), $C_{10}H_9$ (**3**), $C_{14}H_9$ (**4**); L = PPh_3, $Cp' = \eta^5\text{-}C_5H_5$ (**a**); $L_2 = dppe$, $Cp' = \eta^5\text{-}C_5Me_5$ (**b**)]. Whilst the

* Corresponding author. Tel.: +44 191 334 2114; fax: +44 191 384 4737.
E-mail address: p.j.low@durham.ac.uk (P.J. Low).

0022-328X/$ - see front matter © 2007 Elsevier B.V. All rights reserved.
doi:10.1016/j.jorganchem.2007.03.042

17-electron cation radicals derived from the $Ru(PPh_3)_2Cp$ fragment are generally very reactive even on the timescale of the CV experiment, the *para*-tolyl compound [$Ru(C{\equiv}CC_6H_4Me\text{-}4)(PPh_3)_2Cp$] gives rise to an almost completely reversible oxidation, and good quality IR [$\nu(C{\equiv}C)$] and electronic (UV–Vis-NIR) spectra are readily obtained in the absence of atmospheric oxygen and moisture using spectroelectrochemical methods. The complexes featuring the more electron-donating $Ru(dppe)Cp^*$ moiety are relatively stable across the series, and we have succeeded in obtaining good quality spectroscopic data from each compound **1b**, **2b**, **3b** and **4b**. These data are presented and discussed here.

2. Results and discussion

Acetylide complexes [$Ru(C{\equiv}CR)(L_2)(\eta^5\text{-}C_5H_5)$] are conveniently prepared by reactions of the analogous chloride with a terminal alkyne, and deprotonation of the resulting vinylidene [17]. It is also possible to prepare such complexes from trimethylsilyl protected terminal alkynes when the metallation reaction is carried out in the presence of fluoride ions [18]. Together, these methods allow the convenient preparation of not only simple phenyl acetylide complexes such as [$Ru(C{\equiv}CPh)(PPh_3)_2Cp$] (**1a**) [19] and [$Ru(C{\equiv}CPh)(dppe)Cp^*$] (**1b**) [20], but also substituted derivatives far too numerous to list in detail here [13,21–25]. We have used these methods in the preparation of half-sandwich ruthenium acetylide complexes bearing simple aromatic substituents (**1**–**4**) (Chart 1). We note that only a small number of related half-sandwich ruthenium acetylide complexes of fused-ring aromatic alkynes, such as ethynyl naphthalimide and ethynyl pyrone, are known [25]. The iron analogue of **3b** has recently been reported [26].

The IR spectra of complexes **1**–**4** exhibit $\nu(C{\equiv}C)$ bands for the coordinated acetylide moiety at *ca.* 2070 (**1**, **2**), 2055 (**3**) and 2040 (**4**) cm^{-1}, somewhat lower in energy than the organic alkynes [15b,27,28]. It is interesting to note that whilst these IR bands are remarkably insensitive to the other supporting ligands at the metal centre, the $\nu(C{\equiv}C)$ frequency is attenuated by the nature of the aromatic acetylide substituent. The carbons of the acetylide moieties were observed in the ^{13}C NMR spectra as triplets (C_α, $J_{CP} = 25$ Hz) and singlets (C_β). The C_α resonances were progressively deshielded by the larger aromatic substitutent [e.g. δ_C **1b** (128.8) ~ **2b** (126.4) < **3b** (135.1) < **4b** (144.6)]. The Cp and Cp^* ligand resonances were found as singlets in the ^1H and ^{13}C NMR spectra in the usual regions (Cp/Cp^*: $\delta_H = 4.3$–$4.6/1.5$–1.6 ppm; $\delta_C = 85$–$86/10.0$–10.5, 92–93 ppm) whilst the supporting phosphine ligands gave rise to singlets in the ^{31}P NMR spectra at *ca.* 50.5–51.5 (PPh_3) or 81–83 (dppe) ppm.

3. Electrochemical characterisation

Typically, half-sandwich ruthenium acetylides undergo single electron oxidation in common solvents to give the corresponding radical cations. Their redox potentials and chemical stability are sensitive to both the supporting ligands on the ruthenium centre and the acetylide substituent [13,20,21d,25a]. In this work we have examined the anodic behaviour of [$Ru(C{\equiv}CC_6H_5)(L_2)Cp'$] (**1a**,**b**), [$Ru(C{\equiv}CC_6H_4Me\text{-}4)(L_2)Cp'$] (**2a**,**b**), [$Ru(C{\equiv}CC_{10}H_7)(L_2)Cp'$] (**3a**,**b**) and [$Ru(C{\equiv}CC_{14}H_9)(L_2)Cp'$] (**4a**,**b**).

The cyclic voltammogram of [$Ru(C{\equiv}CC_6H_5)(PPh_3)_2Cp$] (**1a**) in dichloromethane is characterised by an oxidation event at 0.59 V (Table 1), the chemical reversibility of which improves at lower temperatures ($i_{pa}{:}i_{pc} = 1.7$ at -78 °C, $v = 100$ mV s^{-1}) and at faster scan rates ($i_{pa}{:}i_{pc} = 1.1$ at -78 °C, $v = 800$ mV s^{-1}). At higher potentials, a second anodic wave was also observed, which was completely irreversible (Table 1). The behaviour of the naphthyl (**3a**) and anthryl (**4a**) substituted derivatives were similar to those described for the phenyl acetylide complex, with the first oxidation event associated with **4a** being rather more thermodynamically favourable (Table 1). The chemical reversibilities of the naphthyl (**3a**) and anthryl (**4a**) substituted derivatives were poor under all conditions examined.

In contrast, the oxidation of the *p*-tolyl compound [$Ru(C{\equiv}CC_6H_4Me\text{-}4)(PPh_3)_2Cp$] (**2a**) proved to be fully chemically reversible at room temperature ($i_{pa}{:}i_{pc} = 1$), with the variation in ΔE_p being no greater than that of

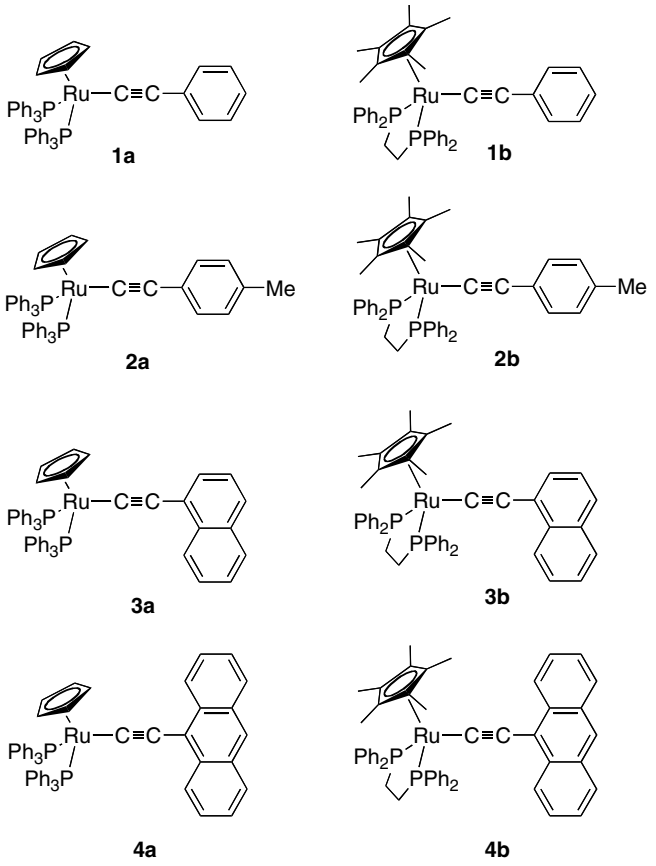

Chart 1. The complexes studied in this work.

Table 1
Electrochemical data for complexes **1**–**4**

	$E^{a}_{(1/2)}$	ΔE^{b}_{p}	i_{pa}:i_{pc}	$E(2)^{c}_{pa}$
1a[d]	0.59	115	1.7	1.39
2a[e]	0.53	120	1.0	1.40
3a[d]	0.55	85	4.3	1.44
4a[d]	0.42	130	7.7	1.60
1b[e]	0.34	80	1.0	1.19
2b[e]	0.31	90	1.0	1.17
3b[e]	0.36	110	1.0	1.28
4b[e]	0.29	90	1.0	1.07

[a] All E values in Volt vs. SCE. Conditions: CH_2Cl_2 solvent, 10^{-1} M NBu_4PF_6 electrolyte, Pt working, counter and pseudo-reference electrodes, $v = 100$ mV s^{-1}. The decamethyl ferrocene/decamethyl ferrocenium F_c^*/F_c^{*+} couple was used as an internal reference for potential measurements F_c^*/F_c^{*+} taken as −0.02 V vs. SCE in CH_2Cl_2/0.1 M $[NBu_4]PF_6$ [29].
[b] $\Delta E_p = |E_{pa} - E_{pc}|$.
[c] Anodic peak potential of a totally irreversible process.
[d] −78 °C.
[e] 20 °C.

the internal decamethyl ferrocene/decamethyl ferrocenium reference couple and independent of scan rate. Plots of i_{pa} vs. $v^{1/2}$ were also linear for this species. This improved chemical reversibility over the compounds **1a**, **3a** and **4a** suggests the involvement of the ring hydrogen in the position *para* to the metal acetylide fragment in at least one of the chemical pathways responsible for the reactivity of the $[Ru(C{\equiv}CAr)(PPh_3)_2Cp]^+$ systems.

The same trend in electrode potentials as a function of the acetylide substituent observed in the $Ru(PPh_3)_2Cp$ series was also apparent in the Ru(dppe)Cp* complexes, with the anthryl derivative being oxidised at significantly lower potentials than the other members of the series **1b**–**4b**. The introduction of the bulky and more electron-donating Cp* and dppe ligands around the ruthenium acetylide framework rendered the first oxidation event of the [Ru(C≡CAr)(dppe)Cp*] series *ca.* 100–200 mV more favourable than the analogous $[Ru(C{\equiv}CAr)(PPh_3)_2Cp]$ complexes. These processes are completely electrochemically and chemically reversible at room temperature and moderate scan rates ($v = 100$ mV s^{-1}), with linear plots of i_{pa} vs. $v^{1/2}$ being obtained and ΔE_p values of comparable magnitude as the internal reference couple (Table 1).

4. IR spectroelectrochemical studies

The reactivity of $[Ru(C{\equiv}CPh)(PPh_3)_2Cp]^+$ (**1a**) implied by the CV study was briefly investigated by spectroelectrochemical methods. For this study, and those which are described in more detail below, we employed an air-tight spectroelectrochemical cell fitted with CaF_2 windows to provide transparency across the spectroscopic region of interest [30]. During rapid oxidation of **1a** the ν(C≡C) band at 2074 cm^{-1}, which is characteristic of the 18-electron ruthenium acetylide, shifted to give rise to a transient species with an IR bands at 1937 and 1529 cm^{-1}. By comparison with results obtained from **2a**, and the Ru(dppe)Cp* series **1b**–**4b** these bands are attributed to $[Ru(C{\equiv}CPh)(PPh_3)_2Cp]^+$ ($[\mathbf{1a}]^+$) (vide infra). However, $[\mathbf{1a}]^+$ proved to be unstable under the conditions of the spectroelectrochemical experiment, and rapidly converted to a second species with IR bands at 2362, 2173 and 1650 cm^{-1}. Whilst the band at 2173 cm^{-1} is in the appropriate region for an organic alkyne, we have not pursued the nature of the decomposition species further. However, we do note that there is no evidence for the formation of the carbonyl cation $[Ru(CO)(PPh_3)_2Cp]^+$, which gives a characteristic ν(CO) band near 1970 cm^{-1} [13].

The greater chemical stability of the [Ru(C≡CAr)(dppe)Cp*] series **1b**, **2b**, **3b** and **4b** under the conditions of the cyclic voltammetry experiments prompted us to consider spectroscopic characterisation of the products derived from their one-electron oxidation more thoroughly by spectroelectrochemical means. Oxidation of **1b** was monitored in both the IR and UV–Vis-NIR spectroscopic regions. The intensity of the characteristic ν(C≡C) band of **1b** at 2072 cm^{-1} decreased, being replaced by a new band at 1929 cm^{-1} as the oxidation proceeded (Table 2). In addition, new bands in the aromatic ν(CC) region were also observed (Table 2). The original spectrum was fully recovered after back-reduction, which confirmed the assignment of the new bands to $[\mathbf{1b}]^+$, and not to some product of an EC process (Fig. 1). This spectroelectrochemical work confirms the tentative assignment of this ν(C≡C) band to $[\mathbf{1b}]^+$ by Paul et al. from chemically oxidised samples of **1b** [13]. The shift of the ν(C≡C) band by 143 cm^{-1} upon oxidation indicates the appreciable

Table 2
IR data (cm^{-1}) for compounds **1b**–**4b** and the corresponding cations[a]

	Neutral species		Oxidised (cation radical) complex	
	ν(CC)	ν(Aryl)	ν(CC)	ν(Aryl)
1b	2072(s)	1593(w)	1929(s)	1614(m), 1551(s), 1540(s), 1520(m)
2a	2077(s)	1606(vw)	1925(s)	1587(s)
2b	2073(s)	1606(w)	1928(s)	1588(s)
3b	2053(s)	1567(w)	1916(s)	1634(m), 1594(m), 1549(s)
4b	2041(s)	1561(vw)	1925(s)	1610(w), 1597(w), 1588(w), 1534(w)

[a] Data from CH_2Cl_2 solutions containing 0.1 M NBu_4BF_4 supporting electrolyte at ambient temperature.

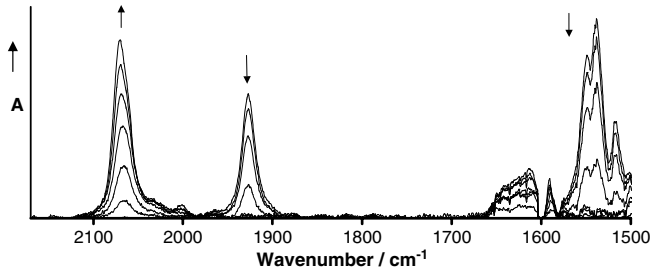

Fig. 1. IR spectra on back reduction of $[\mathbf{1b}]^+$ to **1b** in a spectroelectrochemical cell (CH_2Cl_2/0.1 M NBu_4PF_6, ambient temperature).

depopulation of an orbital with C≡C bonding character. Similar results were obtained from **2b**, **3b** and **4b**, with oxidation resulting in a shift of the ν(C≡C) band by 145, 137 and 116 cm^{-1}, respectively, and with the original spectra being fully recovered after the back-reduction in the spectroelectrochemical cell.

In the case of the remaining members of the $Ru(PPh_3)_2Cp$ series, we note here that the introduction of the *para*-methyl group in **2a** instills significant chemical stability at room temperature to this simple complex. Upon oxidation of **2a**, the ν(C≡C) band at 2077 cm^{-1} shifts by some 150 cm^{-1} to give a new band at 1925 cm^{-1}, which is assigned to the ν(C≡C) band in $[\mathbf{2a}]^+$. The comparable shift in the spectra of **2a**/$[\mathbf{2a}]^+$ compared with **2b**/$[\mathbf{2b}]^+$ is revealing, and implies similar acetylide bonding character in the radical cations, regardless of the electron-donating ability of the supporting ligands.

5. Electronic structure calculations

A theoretical investigation was conducted at the DFT level, initially on the model systems $[Ru(C{\equiv}CC_6H_5)(PH_3)_2Cp]$ (**1-H**) and $[Ru(C{\equiv}CC_{14}H_9)(PH_3)_2Cp]$ (**4-H**), which were used to mimic complexes **1a**, **1b** and **4a**, **4b**, and the corresponding radical cations $[\mathbf{1\text{-}H}]^+$ and $[\mathbf{4\text{-}H}]^+$. The discussion which follows refers to results obtained from calculations at the B3LYP/3-21G* level of theory with no symmetry constraints (Table 3), as results obtained from other functionals and basis sets are in good general agreement (vide infra). There is excellent agreement between the crystallographically determined structures of **1a** [31,32] and **1b** [13] with the DFT optimised geometries determined here, and also with calculations previously reported [13]. Energies and composition of the frontier orbitals are summarised in Table 4 for **1-H**, $[\mathbf{1\text{-}H}]^+$, **4-H** and $[\mathbf{4\text{-}H}]^+$, while Fig. 2 illustrates the labelling scheme.

Table 3
Optimised bond lengths (Å) for **1-H**, $[\mathbf{1\text{-}H}]^+$, **4-H** and $[\mathbf{4\text{-}H}]^+$

	1-H	$[\mathbf{1\text{-}H}]^+$	Δ	**4-H**	$[\mathbf{4\text{-}H}]^+$	Δ
Ru–P(1,2)	2.278	2.324	+0.046	2.280	2.309	+0.029
Ru–C_α	2.018	1.944	−0.074	2.013	1.954	−0.060
$C_\alpha{\equiv}C_\beta$	1.228	1.247	+0.019	1.230	1.246	+0.016
C_β–C(1)	1.426	1.400	−0.026	1.420	1.385	−0.035
C(1)–C(2,6)	1.412	1.423	+0.011	1.425	1.448	+0.023
C(2,6)–C(3,5)	1.392	1.386	−0.006	1.444	1.437	−0.007
C(3,5)–C(4)	1.398	1.403	+0.005	1.400	1.407	+0.007

The Ru–C_α, Ru–P, $C_\alpha{\equiv}C_\beta$ and C_β–C(1) bond lengths in **4-H** are comparable with those found in **1-H**. At the level of theory employed, the aromatic substituents in the neutral systems **1-H** and **4-H** lie in the plane approximately parallel to the Cp ring, although there is a barrier to rotation of the aromatic group around the C(2)–C(3) bond of only *ca.* 0.3 kcal mol^{-1} for **1-H**. In contrast, the plane of the aromatic substituents in the mono-oxidised species $[\mathbf{1\text{-}H}]^+$ and $[\mathbf{4\text{-}H}]^+$ are found approximately bisecting the P–Ru–P angle. The barrier to rotation of the aromatic group around the C(2)–C(3) bond is considerable at *ca.* 6 kcal mol^{-1} for $[\mathbf{1\text{-}H}]^+$.

The electronic structure of **1-H** has been described before [13], and only pertinent details will be summarised here. The HOMO and [HOMO − 1] are approximately orthogonal and derived from mixing of the metal d and acetylide π-systems, with the HOMO also containing appreciable contributions from the phenyl π-system (Table 4, Fig. 3).

Occupied orbitals comprised largely of metal and Cp, metal phosphine and phenyl π-character are found lower in the occupied orbital manifest. The LUMO and [LUMO + 1] of **1-H** are largely Ru–Cp anti-bonding in character, with the phenyl π^* system some 1.35 eV higher in energy than the LUMO, and comprising the [LUMO + 3] (Fig. 4).

The frontier orbitals of **4-H** feature important contributions from the anthryl substituent (Table 4, Fig. 5). Thus, while the HOMO and [HOMO − 1] are approximately orthogonal π-type orbitals, the HOMO features a large (67%) contribution from the atoms of the anthryl substitutent and is somewhat removed from the other occupied orbitals. The LUMO is essentially the anthryl π^* orbital, which is sufficiently low in energy to lie below the unoccupied Ru–Cp based orbitals that comprise the [LUMO + 1] and [LUMO + 2].

The model radical cation $[\mathbf{1\text{-}H}]^+$ features an Ru–C bond somewhat shorter than **1-H** (Table 3). The metal–phosphine bond lengths are sensitive to the net electron density available for π-back bonding and as such are elongated in $[\mathbf{1\text{-}H}]^+$ relative to **1-H**. The elongation of the acetylide C≡C bond in $[\mathbf{1\text{-}H}]^+$ when compared with the neutral model system **1-H** is consistent with a decrease in the net acetylide π-bonding character. This is also supported by the calculated ν(C≡C) frequencies of **1-H** (2058 cm^{-1}) and $[\mathbf{1\text{-}H}]^+$ (1938 cm^{-1}) [33]. The contraction of the C(2)–C(3), C(4)–C(5) and C(7)–C(8) bonds and elongation of the remaining C–C bonds in the phenyl substituent is consistent with the evolution of a degree of cumulenic character in the radical cation. The frontier orbitals of the one-electron oxidation product $[\mathbf{1\text{-}H}]^+$ are similar to those of **1-H**, with the α-HOSO and β-LUSO displaying appreciable Ru(d) and acetylide (π) character and the next highest unoccupied orbitals being largely centred on the $Ru(PH_3)_2Cp$ fragment (Table 4, Fig. 3).

Table 4
Energy, occupancy, and composition of frontier orbitals in the model complexes **1-H**, $[\mathbf{1\text{-}H}]^+$, **4-H** and $[\mathbf{4\text{-}H}]^+$ (B3LYP/3-21G*)

	MO									
	LUMO + 3	LUMO + 2	LUMO + 1	LUMO	HOMO	HOMO − 1	HOMO − 2	HOMO − 3	HOMO − 4	
1-H										
ε (eV)	+0.09	−0.03	−0.15	−0.78	−4.91	−5.09	−5.72	−6.46	−6.65	
Occ	0	0	0	0	2	2	2	2	2	
%Ru	27	53	62	50	30	46	46	0	58	
%Cp	2	3	16	24	2	8	26	0	3	
$\%PH_3$	12	11	13	27	1	4	14	0	8	
$\%C_\alpha$	10	6	8	0	16	10	6	0	4	
$\%C_\beta$	1	2	0	0	22	28	1	0	1	
%Ph	48	26	0	0	29	4	6	100	27	
4-H										
ε (eV)	−0.08	−0.30	−0.92	−1.38	−4.53	−5.32	−5.68	−6.07	−6.25	
Occ	0	0	0	0	2	2	2	2	2	
%Ru	75	60	50	2	11	47	49	36	0	
%Cp	3	17	24	0	1	8	12	17	0	
$\%PH_3$	21	13	27	0	1	4	7	9	0	
$\%C_\alpha$	1	9	0	6	11	9	1	8	0	
$\%C_\beta$	0	0	0	0	8	25	8	13	0	
%Anth	0	0	0	91	67	7	23	18	100	

	MO																	
	88β	88α	87β	87α	86β	86α	85β	85α	84 β	84α	83 β	83α	82 β	82α	81 β	81α	80 β	80α
	β-[LUSO + 4]	α-[LUSO + 3]	β-[LUSO + 3]	α-[LUSO + 2]	β-[LUSO + 2]	α-[LUSO + 1]	β-[LUSO + 1]	α-LUSO	β-LUSO	α-HOSO	β-HOSO	α-[HOSO − 1]	β-[HOSO − 1]	α-[HOSO − 2]	β-[HOSO − 2]	α-[HOSO − 3]	β-[HOSO − 3]	α-[HOSO − 4]
$[\mathbf{1\text{-}H}]^+$																		
ε(eV)	−3.28	−3.29	−3.67	−4.03	−4.15	−4.26	−4.82	−4.95	−7.27	−9.00	−9.51	−9.67	−9.85	−9.95	−9.92	−10.19	−10.08	−10.41
Occ	0	0	0	0	0	0	0	0	0	1	1	1	1	1	1	1	1	1
%Ru	64	64	7	5	55	53	48	47	33	23	51	50	41	39	29	0	0	20
%Cp	2	2	3	1	20	20	26	27	6	7	3	4	29	37	17	0	0	29
$\%PH_3$	33	34	2	2	16	15	26	26	4	4	2	2	10	11	6	0	0	9
$\%C_\alpha$	0	0	16	19	9	10	0	0	10	11	11	11	8	7	11	0	0	6
$\%C_\beta$	0	0	3	7	1	1	0	0	21	16	30	29	3	5	0	0	0	0
%Ph	0	0	70	68	0	0	0	0	26	38	4	3	9	1	37	100	100	35

	MO																	
	114β	114α	113β	113α	112β	112α	111β	111α	110β	110α	109β	109α	108β	108α	107β	107α	106β	106α
	β-[LUSO + 4]	α-[LUSO + 3]	β-[LUSO + 3]	α-[LUSO + 2]	β-[LUSO + 2]	α-[LUSO + 1]	β-[LUSO + 1]	α-LUSO	β-LUSO	α-HOSO	β-HOSO	α-[HOSO − 1]	β-[HOSO − 1]	α-[HOSO − 2]	β-[HOSO − 2]	α-[HOSO − 3]	β-[HOSO − 3]	α-[HOSO − 4]
$[\mathbf{4\text{-}H}]^+$																		
ε (eV)	−3.13	−3.27	−3.63	−3.71	−4.28	−4.35	−4.73	−5.12	−6.78	−8.08	−8.75	−9.11	−9.03	−9.22	−9.37	−9.43	−9.67	−9.74
Occ	0	0	0	0	0	0	0	0	0	1	1	1	1	1	1	1	1	1
%Ru	0	0	56	55	49	48	4	3	17	12	30	55	56	32	43	40	0	0
%Cp	0	0	20	20	26	26	1	1	3	3	8	8	6	14	29	29	0	0
$\%PH_3$	0	0	15	15	25	26	1	1	2	2	4	4	4	6	11	10	0	0
$\%C_\alpha$	0	0	9	9	0	0	8	9	10	8	0	7	7	1	7	8	0	0
$\%C_\beta$	0	0	1	1	0	0	0	0	10	8	11	22	22	11	8	10	0	0
%Anth	100	100	0	0	0	0	87	87	58	67	46	5	4	37	2	2	100	100

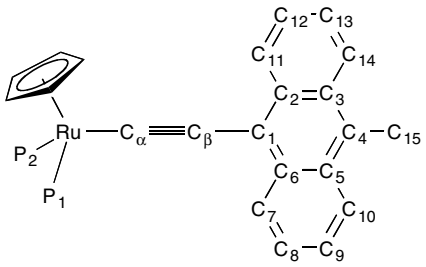

Fig. 2. The labelling scheme used in the discussion of the DFT results, and ^{13}C NMR spectra.

The optimised geometry of $[\mathbf{4\text{-}H}]^+$ displays elongated Ru–P bond lengths and evidence of an increased cumulenic character in the ethynyl anthryl portion of the molecule when compared with the bond distances in **4-H** (Table 3). While the trends in the structures and calculated ν(C≡C) frequencies of [**4-H**] [ν(C≡C) = 2038 cm^{-1}] and $[\mathbf{4\text{-}H}]^+$ [ν(C≡C) = 1952 cm^{-1}] follow those observed for **1-H** and $[\mathbf{1\text{-}H}]^+$, it is interesting to compare the pairs of structures **1-H**/$[\mathbf{1\text{-}H}]^+$ and **4-H**/$[\mathbf{4\text{-}H}]^+$ and note the relative differences in the individual bond lengths (Table 3). Although the magnitude of individual deviations are small (<0.05 Å) there is a clear trend indicating that the anthryl fragment in $[\mathbf{4\text{-}H}]^+$ experiences a greater relative structural distortion than the phenyl ring in $[\mathbf{1\text{-}H}]^+$. Conversely, the metal ethynyl fragment is more significantly affected in $[\mathbf{1\text{-}H}]^+$ than in $[\mathbf{4\text{-}H}]^+$, which is neatly reflected in the differences between the ν(C≡C) frequencies of the 18- and 17-electron compounds in both the experimental (**1b**/$[\mathbf{1b}]^+$ $\Delta\nu$(C≡C) = 143 cm^{-1}; **4b**/$[\mathbf{4b}]^+$ $\Delta\nu$(C≡C) = 116 cm^{-1}) and model systems [**1-H**/$[\mathbf{1\text{-}H}]^+$ $\Delta\nu$(C≡C) = 120 cm^{-1}; **4-H**/$[\mathbf{4\text{-}H}]^+$ $\Delta\nu$(C≡C) = 86 cm^{-1}].

The frontier orbitals of $[\mathbf{4\text{-}H}]^+$ are similar to those of **4-H**. The α-HOSO and α-LUSO of $[\mathbf{4\text{-}H}]^+$ offer an appreciable anthryl character (α: 67%, 87%, respectively). It may therefore be more appropriate to consider species such as $[\mathbf{4b}]^+$ as metal-stabilised anthryl radicals. The optimised geometries of **4-H** and $[\mathbf{4\text{-}H}]^+$ supported this point of view, as do calculated spin densities, with the atoms comprising the anthryl ring system contributing some 60% of the fractional electronic charge in $[\mathbf{4\text{-}H}]^+$ compared with the phenyl ring system contribution of some 25% in $[\mathbf{1\text{-}H}]^+$ (Table 5).

6. UV–Vis spectroelectrochemical studies

Comparison of the electronic absorption spectra of **1b**, **2b**, **3b** and **4b** reveals a strong, and in the case of **4b**, relatively narrow, absorption band between 33 000 and

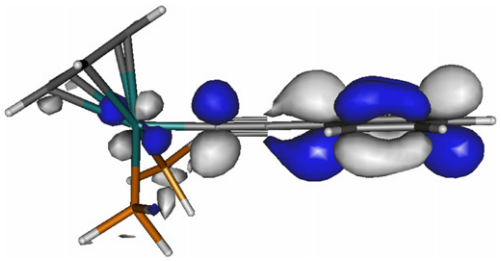

Fig. 4. The [LUMO + 3] of **1-H** plotted with contour values ±0.04 (e/bohr^3)$^{1/2}$.

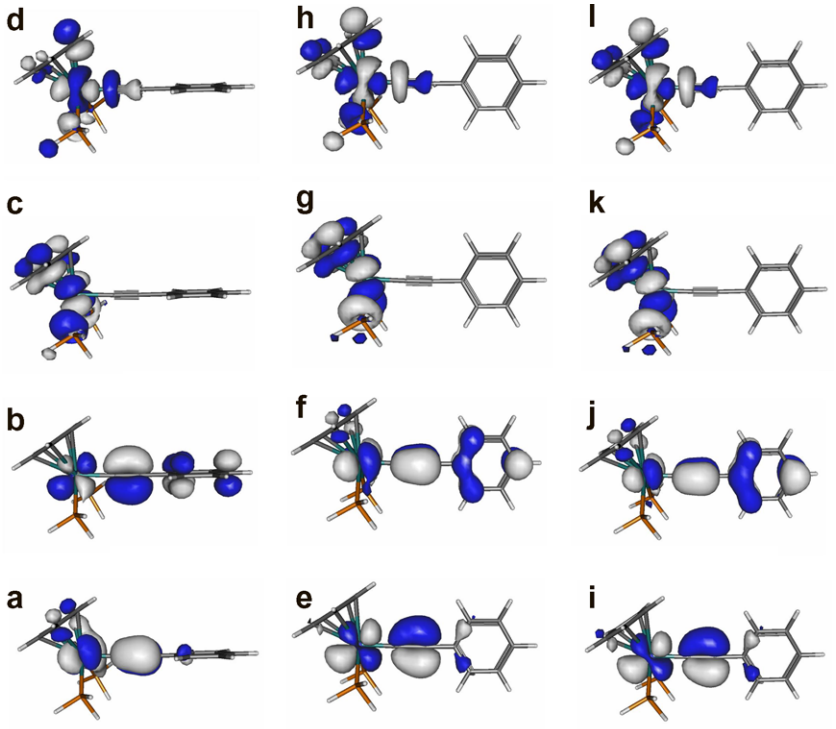

Fig. 3. The (a) [HOMO − 1], (b) HOMO, (c) LUMO, (d) [LUMO + 1] of **1-H** together with (e) β-HOSO, (f) β-LUSO, (g) β-[LUSO + 1], (h) β-[LUSO + 2] of $[\mathbf{1\text{-}H}]^+$ and (i) α-[HOSO − 1], (j) α-HOSO, (k) α-LUSO, (l) α-[LUSO + 1] of $[\mathbf{1\text{-}H}]^+$ plotted with contour values ±0.04 (e/bohr^3)$^{1/2}$.

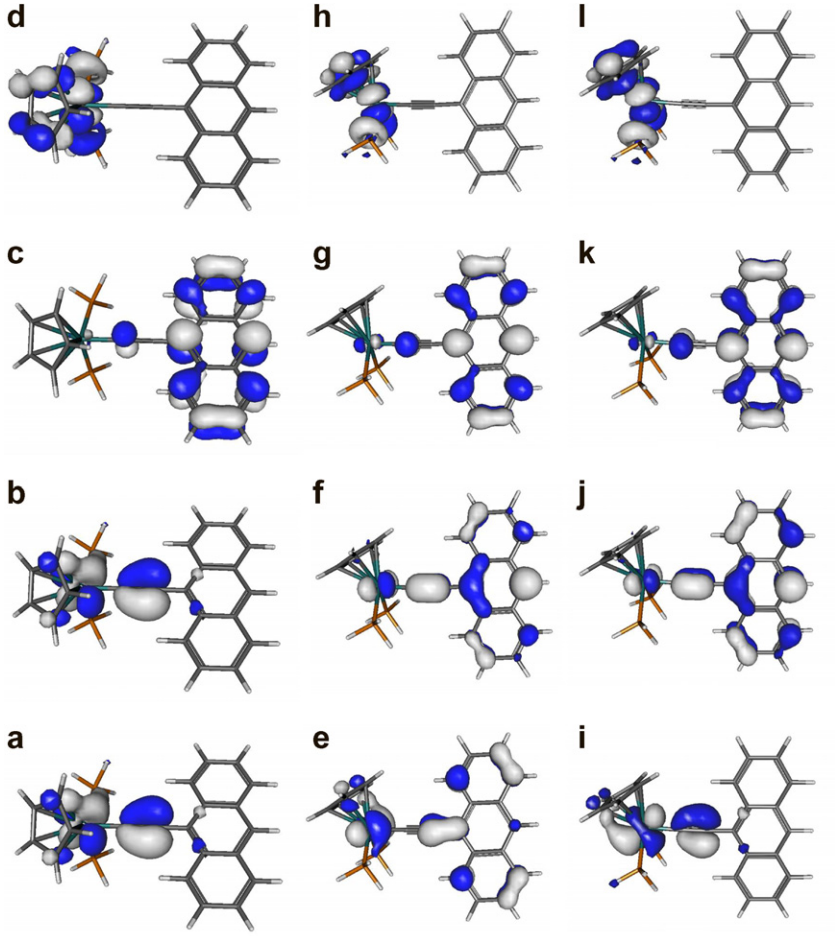

Fig. 5. The (a) [HOMO − 1], (b) HOMO, (c) LUMO, (d) [LUMO + 1] of **4-H** together with (e) β-HOSO, (f) β-LUSO, (g) β-[LUSO + 1], (h) β-[LUSO + 2] of $[\mathbf{4\text{-}H}]^+$ and (i) α-[HOSO − 1], (j) α-HOSO, (k) α-LUSO, (l) α-[LUSO + 1] of $[\mathbf{4\text{-}H}]^+$ plotted with contour values ±0.04 $(e/bohr^3)^{1/2}$.

Table 5
Spin densities computed for the model radical cations, $[\mathbf{1\text{-}H}]^+$ and $[\mathbf{4\text{-}H}]^+$

	$[\mathbf{1\text{-}H}]^+$	$[\mathbf{4\text{-}H}]^+$	Δ
Ru	0.413	0.220	0.193
P	0.000	0.000	0.000
Cp	0.041	0.021	−0.079
C_α	0.043	0.079	−0.036
C_β	0.269	0.114	0.155
$C_6H_5/C_{14}H_9$	0.246	0.598	−0.352

Table 6
The principal UV–Vis absorption bands $[\bar{\nu}_{max}/cm^{-1}(\varepsilon_{max}/M^{-1}cm^{-1})]$ observed from $CH_2Cl_2/10^{-1}$ M NBu_4PF_6 solutions of $[\mathbf{1b}]^{n+}$, $[\mathbf{2a}]^{n+}$, $[\mathbf{2b}]^{n+}$, $[\mathbf{3b}]^{n+}$ and $[\mathbf{4b}]^{n+}$ ($n = 0, 1$)

	n	
	0	+1
1b	29 500 (9500)	22 600 (3900), 21 100 (4300), 11 200 (5100), 8100 (600)
2a	30 700 (7000)	30 300 (4500), 19 100 (1200), 14 300 (1500), 11 900 (900), 7500 (100)
2b	33 400 (7000)	29 800 (4500), 26 200 (2700), 16 900 (800), 13 900 (1800), 8600 (200)
3b	26 200 (7000)	20 200 (3100), 18 600 (2500), 11 000 (3900), 7600 (700)
4b	20 600 (11 600)	27 200 (8000), 17 900 (14 000), 15 200 (5900), 10 100 (1900), 7800 (600)

20 000 cm^{-1}, which becomes progressively red-shifted as a function of the size of the aromatic substituent and accounts for the colour of these complexes (Table 6, Figs. 6 and 8). The analogous bands in [Ru(C≡CC_6H_4X-4)(dppe)Cp*] (X = H, CN, F, OMe, NH_2) have been assigned to MLCT processes by analogy with assignments made for iron complexes [13]. Although electronic structure calculations on [Ru(C≡CPh)(PH_3)Cp] model systems have been performed on previous occasions [13,14], only limited use has been made of TD DFT based studies to provide further insight into the nature of the electronic transitions responsible for the characteristic absorption spectra of related systems [21a,34,35].

On the basis of TD DFT calculations the characteristic absorption band observed in **1b**, and by analogy **2b** and **3b**, can be likened, in the most general terms, to a (d/π) – phenyl π* charge transfer band ($HOMO \rightarrow [LUMO + 3]$) rather than a purely MLCT band. In the case of **4b** there is a critical distinction and the band at 20 600 is better described as an anthryl-centred π–π* transition ($HOMO \rightarrow LUMO$). This distinction in assignment is consistent with the different band shapes observed for **1b**–**3b** on one hand, and **4b** on the other (Figs. 6 and 8).

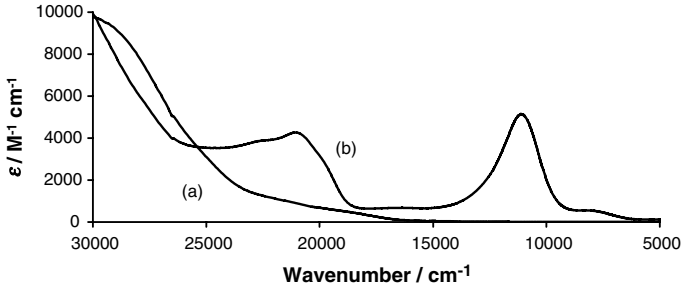

Fig. 6. The UV–Vis-NIR spectra of (a) **1b** and (b) $[\mathbf{1b}]^+$ (CH_2Cl_2/0.1 M NBu_4PF_6).

The UV–Vis-NIR spectrum of $[\mathbf{1b}]^+$, obtained spectroelectrochemically from **1b**, exhibits strong absorption envelopes centred near 21 100 and 11 200 cm^{-1}, and a weaker series of bands between 8000 and 4000 nm (Fig. 6). The spectrum of **1b** was fully recovered after back-reduction, which strongly supports the assignment of these characteristic absorption bands to the 17-e species $[\mathbf{1b}]^+$. TD DFT calculations using the $[\mathbf{1\text{-}H}]^+$ model indicate that the highest energy transition can be attributed to charge transfer from the metal fragment (including the acetylide π-system) to the phenyl (π^*) ring being comprised of electronic transitions from the α-HOSO (highest occupied spin orbital) to the α-[LUSO]. The band centred near 11 200 cm^{-1} can be approximated in terms of transitions between occupied orbitals with large amounts of Ru/Cp character (β-[HOSO − 1], β-[HOSO − 2], Table 4, Fig. 7) to the β-LUSO. The presence of low energy (NIR) bands in 17-e cation radicals of the general type $[Ru(C{\equiv}CAr)(dppe)Cp^*]^+$ has been noted by Paul *et al.*, and attributed to forbidden ligand-field type transitions centred on the Ru(III) centre [13]. The TD DFT calculations carried out in the present study suggest that the lowest energy transition should be attributed to the β-HOSO to β-LUSO transition, with the low intensity of the observed band reproduced by the low calculated oscillator strength and easily explained by the relative, approximately orthogonal orientation of these two orbitals. Other NIR bands of slightly greater intensity and higher energy are attributable to Ru/Cp based β-[HOSO − 1] to the β-LUSO.

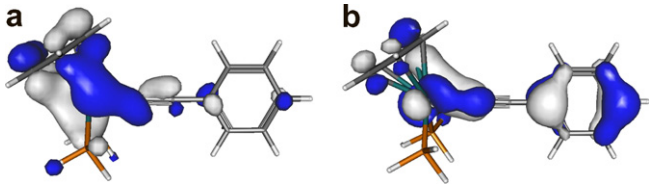

Fig. 7. The (a) β-[HOSO − 1] and (b) β-[HOSO − 2] of $[\mathbf{1\text{-}H}]^+$ plotted with contour values ±0.04 $(e/bohr^3)^{1/2}$.

The tolyl-substituted derivatives $[\mathbf{2a}]^+$ and $[\mathbf{2b}]^+$, and the naphthyl derivative $[\mathbf{3b}]^+$ offer similar electronic spectra to each other, and that of $[\mathbf{1b}]^+$. Low NIR energy bands are observed, together with a more intense band envelope in the visible region, the precise shape and composition of which vary only slightly with the nature of the Cp′ and phosphine co-ligands. In the case of $[\mathbf{3b}]^+$ the characteristic absorption bands are somewhat red-shifted compared with the analogous features in $[\mathbf{1b}]^+$, $[\mathbf{2a}]^+$ and $[\mathbf{2b}]^+$. Given the similar profiles of these compounds, and the similar chemical behaviour of each member of the series, we are reasonably confident in attributing these spectroscopic absorption bands to transitions similar to those described for $[\mathbf{1\text{-}H}]^+$.

The anthryl derivative $[\mathbf{4b}]^+$ offers four principal absorption bands near 27 000, 18 200, 15 000 and 10 000 cm^{-1}, together with weaker bands tailing further into the NIR region (Fig. 8). On the basis of TD DFT calculations using

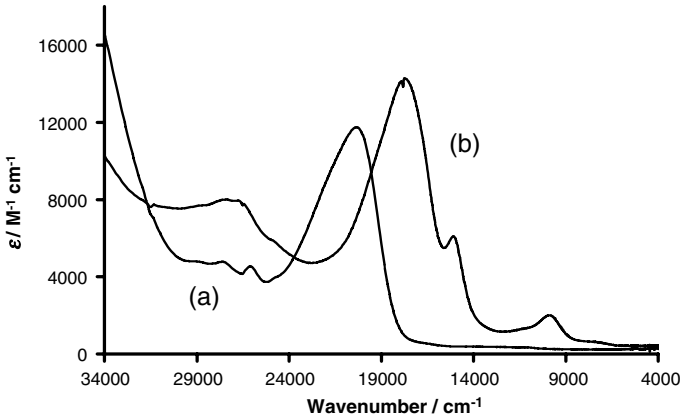

Fig. 8. The UV–Vis-NIR spectra of (a) **4b** and (b) $[\mathbf{4b}]^+$ (CH_2Cl_2/0.1 M NBu_4PF_6).

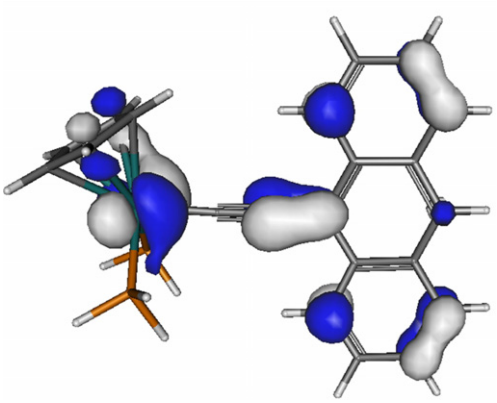

Fig. 9. The β-[HOSO − 4] of $[\mathbf{4\text{-}H}]^+$ plotted with contour values ±0.04 $(e/bohr^3)^{1/2}$.

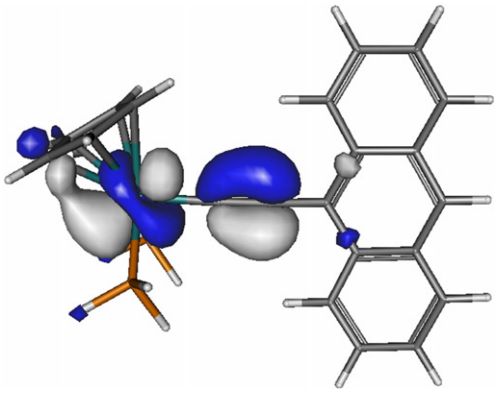

Fig. 10. The β-[HOSO − 1] of $[\mathbf{4\text{-}H}]^+$ plotted with contour values ±0.04 $(e/bohr^3)^{1/2}$.

$[\mathbf{4\text{-}H}]^+$ as a model, the highest-energy band observed in the UV–Vis-NIR spectrum of $[\mathbf{4b}]^+$ is due to electronic excitations from the largely metal/ethynyl based β-HOSO and α-[HOSO − 2] to the β-[LUSO + 1] and α-[LUSO], which are anthracene π^* in character. The intense band at 18 200 cm^{-1} is comprised of electronic transitions between α-HOSO and α-LUSO (i.e. the anthryl radical π–π^* transition), and is red-shifted from the analogous band in **4b**. The less intense band at 15 200 cm^{-1} is largely associated with electronic excitation from the β-[HOSO − 4] to the β-LUSO (Fig. 9), and is approximately an MLCT band.

A relatively intense NIR band ($\lambda_{max} = 10\,000\ cm^{-1}$, $\varepsilon_{max} = 2000\ M^{-1}\ cm^{-1}$) is calculated to arise from excitations involving occupied orbitals with the metal–ethynyl–anthryl character (β-HOSO and α-HOSO) and the β-LUSO and α-LUSO, which are both rather more heavily centred on the anthryl ring systems (Fig. 5). The very weak NIR bands found at even longer wavelengths are assigned to metal to anthryl charge transfer processes, involving excitations largely between the β-[HOSO − 1] and β-LUSO (Fig. 10). The critical distinction between the assignments of the optical transitions in compounds modelled by $[\mathbf{1\text{-}H}]^+$ and $[\mathbf{4\text{-}H}]^+$ is the greater localisation of the β-LUSO and α-HOSO on the aromatic ring in the anthracene derivative.

As a test of the reliability of the B3LYP/3-21G* calculations presented above, the geometry optimisation, frequency calculations and TD DFT calculations on the models [**1-H**] and $[\mathbf{1\text{-}H}]^+$ were repeated using a range of other functionals and basis sets (Table 7). There is a little significant variation in the optimised geometries with computational method. The electronic structures calculated from these various methods are largely consistent, with perhaps the most notable feature being the relative order of the predominantly metal centred orbitals lying below the β-HOSO in $[\mathbf{1\text{-}H}]^+$.

Time-dependent density functional theory calculations of the first vertical transition energies of both the neutral and monocationic models are particularly revealing. Whilst the energy of electronic transitions computed using the different methods varies significantly, the net assignment of the absorption spectra is the same regardless of the functional or basis set employed. Given the gas-phase nature of the calculation and the use of static model systems, the strong electrolyte solution used in the spectroelectrochemical measurement of the absorption spectra and the likely low energy barriers to rotation of the aromatic acetylide substituent around the acetylide–aromatic single bond, it is not possible to pass comment on the true precision of the various computational methods. It is clear, however, that the computationally expedient B3LYP/3-21G* calculations are not significantly less accurate than any of the higher level calculations also examined.

As a further test of the reliability of the calculations, the compounds $[\mathbf{1b}]^{n+}$ and $[\mathbf{4b}]^{n+}$ were also studied using B3LYP/3-21G*, the results of which are summarised in Tables 8 and 9, together with the experimental data and that from the models [**1-H**] and [**4-H**] for ease of comparison. The agreement between the data calculated from the systems containing the full ligand sets and those observed experimentally is better than obtained from any of the calculations using the model ligand sets. However, the assignments of the electronic absorption bands in the experimental systems $[\mathbf{1b}]^{n+}$ and $[\mathbf{4b}]^{n+}$ are not significantly changed.

7. Conclusion

One-electron oxidation of the half-sandwich bis(phosphine) ruthenium acetylide complexes [Ru(C≡CAr)(L_2)Cp′] affords the corresponding radical cations [Ru(C≡CAr)(L_2)Cp′]$^+$. These cations are sensitive to atmospheric conditions. However, the stability of these species is improved through the use of *p*-tolyl acetylide substituents or the bulky Ru(dppe)Cp* metal end-cap and *in situ* spectroelectrochemical methods may be used to record the infrared and UV–Vis-NIR spectra of these relatively 'reactive' cations. The compounds derived from phenylacetylene, 4-ethynyltoluene and 1-ethynylnapthalene offer frontier orbitals with appreciable metal character, which in the case of the HOMO is also admixed with the ethynyl and aromatic π system. There is a critical distinction in the

Table 7
Optimised bond lengths, important vibration frequencies and major electronic excitations for **1-H**, $[\mathbf{1\text{-}H}]^+$, [**1b**] and $[\mathbf{1b}]^+$ determined by TD DFT methods using different functionals and basis sets, with selected experimental data for comparison

	Expt $[\mathbf{1b}]^{n+}$ [13]	B3LYP/3-21G*$[\mathbf{1\text{-}H}]^{n+}$	B3LYP/Gen $[\mathbf{1\text{-}H}]^{n+}$	B3LYP/Gen2 $[\mathbf{1\text{-}H}]^{n+}$	PBE1PBE/3-21G* $[\mathbf{1\text{-}H}]^{n+}$	PBE1PBE/Gen $[\mathbf{1\text{-}H}]^{n+}$	P86/3-21G* $[\mathbf{1\text{-}H}]^{n+}$	BP86/Gen $[\mathbf{1\text{-}H}]^{n+}$	B3LYP/3-21G* $[\mathbf{1b}]^{n+}$
Bond lengths/Å									
$n = 0$									
Ru–C	2.011(4)	2.018	2.028	2.011	1.999	2.010	2.003	2.012	2.015
C≡C	1.215(5)	1.228	1.229	1.222	1.228	1.229	1.242	1.244	1.231
C–Ph	1.431(5)	1.426	1.428	1.424	1.423	1.425	1.426	1.427	1.425
Ru–P	2.262(1), 2.256(1)	2.278	2.291	2.310	2.250	2.264	2.260	2.273	2.287
$n = 1$									
Ru–C		1.944	1.946	1.932	1.929	1.929	1.943	1.942	1.957
C≡C		1.246	1.250	1.241	1.248	1.251	1.260	1.263	1.243
C–Ph		1.400	1.403	1.399	1.397	1.400	1.404	1.406	1.411
Ru–P		2.324	2.335	2.356	2.283	2.299	2.294	2.311	2.350
Vibrational frequencies (IR)/cm^{-1} (intensity)									
$n = 0$									
C≡C	2072(s)	2101 (218)	2084 (248)	2081 (327)	2121 (230)	2108 (256)	2020 (318)	2005 (330)	2077 (374)
Ring	1593(m,w)	1547 (54)	1573 (64)	1556 (76)	1568 (54)	1599 (61)	1494 (71)	1523 (80)	1545 (68)
$n = 1$									
C≡C	1929(s)	1980 (310)	1965 (209)	1906 (271)	1993 (339)	1983 (210)	1920 (29)	1910 (14)	1952 (520)
Ring	1551(m)	1529 (291)	1551 (290)	1537 (298)	1548 (310)	1574 (309)	1482 (165)	1508 (161)	1496 (91)

electronic structure of the compounds based on 9-ethynylanthracene, which instead feature frontier orbitals largely localised on the anthracene moiety. Thus compounds such as $[\mathbf{4b}]^+$ might be better regarded as metal-stabilised anthryl radicals than as radical cations derived from oxidation of the metal centre.

8. Experimental

All reactions were carried out under an atmosphere of nitrogen using standard Schlenk techniques. Reaction solvents were purified and dried using an Innovative Technology SPS-400, and degassed before use. No special precautions were taken to exclude air or moisture during work-up. The compounds [RuCl(PPh_3)Cp] [36], [RuCl(dppe)Cp*] [37], [Ru(C≡CPh)(PPh_3)Cp] [38], [Ru(C≡CC_6H_4-Me-4)(dppe)Cp*] [39], Ru(C≡CPh)(dppe)Cp* [20] and 1-trimethylsilylethynylanthracene (purified by column chromatography on silica gel, eluting with hexane) [40], were prepared by the literature methods. Other reagents, including 4-ethynylnaphthalene (Aldrich) and 4-ethynyltoluene (Aldrich) were purchased and used as received.

NMR spectra were recorded on a Bruker Avance (^{1}H 400.13 MHz, ^{13}C 100.61 MHz, ^{31}P 161.98 MHz) or Varian Mercury (^{31}P 161.91 MHz) spectrometers from $CDCl_3$ solutions and referenced against solvent resonances (^{1}H, ^{13}C) or external H_3PO_4 (^{31}P). IR spectra were recorded using a Nicolet Avatar spectrometer from solutions in a cell fitted with CaF_2 windows. Electrospray ionisation mass spectra were recorded using Thermo Quest Finnigan Trace MS-Trace GC or WATERS Micromass LCT spectrometers. Samples in dichloromethane (1 mg/mL) were 100 times diluted in either methanol or acetonitrile, and analysed with source and desolvation temperatures of 120 °C, with cone voltage of 30 V. High resolution spectra were recorded using a Thermo Electron Finnigan LTQ FT mass spectrometer with capillary temperature 275 °C and capillary voltage 100 V. MALDI-TOF spectra were recorded using an ABI Voyager STR spectrometer, with a 337 nm desorption laser, linear flight path and 2500 V accelerating voltage and *trans*-2-[3-(4-*tert*-Butylphenyl)-2-methyl-2-propenylidene]maleonitrile (DCTB), purchased from Sigma–Aldrich, used as matrix. Samples were prepared from solutions containing 10 mg/1 L of the matrix and 1 mg/1 L of the sample and mixed 1:9 sample:matrix. Only 1 μL of the mixtures was used for analyses.

Cyclic voltammograms were recorded at $v = 100$–800 mV s^{-1} from solutions of approximately 10^{-4} M in analyte in dichloromethane containing 10^{-1} M NBu_4PF_6, using a gastight single-compartment three-electrode cell equipped with platinum disk working, coiled platinum wire auxiliary, and platinum wire pseudo-reference electrodes. The working electrode surface was polished before scans with an alumina paste. The cell was connected to a computer-controlled Autolab PGSTAT-30 potentiostat. All redox potentials are reported against the saturated calomel electrode, and referenced against the decamethylferrocene/decamethylferrocenium F_c^*/F_c^{*+} redox couple used as an internal reference system [29]. Cyclic voltammetric measurements at sub-ambient temperatures were performed with the electrochemical cell immersed into a bath of acetone/dry ice.

UV–Vis-NIR and IR spectroelectrochemical experiments at room temperature were performed with an airtight optically transparent thin-layer electrochemical (OTTLE) cell equipped with a Pt minigrid working electrode (32 wires cm^{-1}) and CaF_2 windows [30]. The cell was positioned in the sample compartment of either a Nicolet Avatar spectrometer (1 cm^{-1} spectral resolution, 16 scans) or a Perkin–Elmer Lambda 900 spectrophotometer. The controlled-potential electrolyses were carried out with a homebuilt potentiostat.

8.1. Complex *1a*

^{13}C NMR ($CDCl_3$, 100 MHz) for **1a**: δ 85.2 (Cp); 114.4 (C_β); 116.1 (t, $J_{CP} = 25$ Hz, C_α); 123.0 (C4), 127.6 (C3); 130.5 (C2); 130.6 (C1); 127.2 (dd, $^3J_{CP}/^6J_{CP} \sim 5$ Hz, C_m); 128.4 (C_p); 133.9 (dd, $^2J_{CP}/^5J_{CP} \sim 5$ Hz, C_o); 139.0 (dd, $^1J_{CP}/^4J_{CP} \sim 11$ Hz C_i).

Table 8
The major electronic excitations for **1-H**, $[\mathbf{1\text{-}H}]^+$, **1b** and $[\mathbf{1b}]^+$ determined by TD DFT methods using different functionals and basis sets, with selected experimental data for comparison

	Expt $[\mathbf{1b}]^{n+}$	B3LYP/3-21G* $[\mathbf{1\text{-}H}]^{n+}$	B3LYP/Gen $[\mathbf{1\text{-}H}]^{n+}$	B3LYP/Gen2 $[\mathbf{1\text{-}H}]^{n+}$	PBE1PBE/3-21G* $[\mathbf{1\text{-}H}]^{n+}$	PBE1PBE/Gen $[\mathbf{1\text{-}H}]^{n+}$	BP86/3-21G* $[\mathbf{1\text{-}H}]^{n+}$	BP86/Gen $[\mathbf{1\text{-}H}]^{n+}$	B3LYP/3-21G* $[\mathbf{1b}]^{n+}$
Electronic transitions/cm^{-1} (Molar extinction coefficient/M^{-1} cm^{-1} or calculated oscillator strength, <1)									
$n = 0$									
HOMO → [LUMO + 3]	29 500 (9500)	37 200 (0.4290)	34 600 (0.1740)[a]	33 900 (0.2115)	37 900 (0.3848)[b]	36 500 (0.4345)[b]	31 300 (0.4735)	30 600 (0.4370)	33 900 (0.1103)[d]
$n = 1$									
β-HOSO → β-LUSO	8100 (600)	6300 (0.0001)	6000 (0.0001)	5700 (0.0001)	6700 (0.0000)	6300 (0.0000)	6000 (0.0001)	5500 (0.0001)	5200 (0.0010)
β-[HOSO − 2] → β-LUSO	11 200	16 200 (0.2661)	16 200	16 000 (0.2583)	16 700 (0.2739)	16 700 (0.2540)	16 400 (0.2081)[c]	16 400 (0.1992)[c]	14 100 (0.0731)
β-[HOSO − 1] → β-LUSO	(5100)		(0.2610)						
α-HOSO → α-LUSO	21 100 (4300)	22 500 (0.0067)	22 700 (0.0067)	22 500 (0.0074)	24 800 (0.0082)	25 600 (0.0044)	20 400 (0.0038)	20 400 (0.0043)	23 900 (0.0072)

[a] *HOMO* → [*LUMO* + 2].
[b] *HOMO* → [*LUMO* + 1].
[c] β-[*HOSO* − 3] → β-*LUSO*.
[d] [*HOMO* − 1] → [*LUMO* + 9].

8.2. Preparation of *[Ru(C≡CC$_6$H$_4$Me-4)(PPh$_3$)$_2$Cp]* (**2a**)

A suspension of $[RuCl(PPh_3)_2Cp]$ (200 mg, 0.28 mmol), $HC{\equiv}CC_6H_4Me$ (32 mg, 0.28 mmol) and NH_4PF_6 (45 mg, 0.28 mmol) in MeOH (15 mL) was heated at reflux for 20 min to form a bright red solution, 2–3 drops of 1,8-Diazabicyclo[5.4.0]undec-7-ene (DBU) were added to form yellow precipitate which was collected by filtration, washed with cold MeOH, and air-dried to afforded **2a** as a yellow solid (125 mg, 56%). IR(Nujol): ν(C≡C) 2076 cm^{-1}. ^{1}H NMR ($CDCl_3$, 400 MHz): δ 2.30 (s, 3H, Me), 4.31 (s, 5H, Cp), 6.95–7.52 (m, 34H, Ar). $^{31}P\{^1H\}$ NMR ($CDCl_3$, 162 MHz): δ 50.6 (s, PPh_3). $^{13}C\{^1H\}$ NMR ($CDCl_3$, 100 MHz): δ 21.2 (Me), 85.1 (Cp); 113.5 (t, $J_{CP} = 25$ Hz, C_α); 114.0 (C_β); 127.8 (CH), 128.4, 130.3 (CH), 132.3 (C1–C4); 127.2 (dd, $^3J_{CP}/^6J_{CP} \sim 5$ Hz, C_m); 128.3 (C_p); 133.9 (dd, $^2J_{CP}/^5J_{CP} \sim 5$ Hz, C_o); 139.1 (dd, $^1J_{CP}/^4J_{CP} \sim 11$ Hz C_i). MALDI-TOF(+)-MS (*m*/*z*): 806, $[M^+]$. High resolution (*m*/*z*): calculated for $RuP_2C_{50}H_{43}$ $[M + H]^+$ 807.18780; found 807.18698.

8.3. Preparation of *[Ru(C≡CC$_{10}$H$_7$)(PPh$_3$)$_2$Cp]* (**3a**)

A suspension of $[RuCl(PPh_3)_2Cp]$ (200 mg, 0.275 mmol), NH_4PF_6 (100 mg, 0.613 mmol) and $HC{\equiv}CC_{10}H_7$ (50 mg, 0.329 mmol) in methanol (20 mL) was heated at reflux for 90 min under a nitrogen atmosphere. The red/orange solution formed was treated with a methanolic solution of NaOMe and the yellow precipitate formed collected, washed with MeOH and hexane and dried to give **3a** as a yellow powder (167 mg, 72%). IR(Nujol): ν(C≡C) 2057 cm^{-1}. ^{1}H NMR ($CDCl_3$, 200 MHz): δ 4.59 (s, 5H, Cp); 8.58–7.10 (m, 37H, Ph, $C_{10}H_7$). $^{31}P\{^1H\}$ NMR ($CDCl_3$, 81 MHz): δ 51.56 (s, PPh_3). $^{13}C\{^1H\}$ NMR ($CDCl_3$, 100 MHz): δ 85.5 (Cp); 112.5 (C_β); 122.6 (t, $J_{CP} = 25$ Hz, C_α);122.8 (CH), 124.8 (CH), 125.3 (CH), 125.8 (CH), 127.4, 127.7 (CH), 128.1 (CH), 128.4, 133.7 (CH), 134.6 (C1–C10); 127.3 (dd, $^3J_{CP}/^6J_{CP} \sim 5$ Hz, C_m); 128.5 (C_p); 133.9 (dd, $^2J_{CP}/^5J_{CP} \sim 5$ Hz, C_o); 139.0 (dd, $^1J_{CP}/^4J_{CP} \sim 11$ Hz, C_i). ES(+)-MS (*m*/*z*): 842, $[M^+]$. High resolution: calculated for $RuP_2C_{53}H_{43}$ $[M + H]^+$ 843.18780; found 843.19002.

8.4. Preparation of *[Ru(C≡CC$_{14}$H$_9$)(PPh$_3$)$_2$Cp]* (**4a**)

A suspension of $[RuCl(PPh_3)_2Cp]$ (200 mg, 0.28 mmol), $Me_3SiC{\equiv}CC_{14}H_9$ (75 mg, 0.28 mmol) and KF (30 mg, 0.56 mmol) in methanol (20 mL) was heated and the orange solution formed allowed to reflux for 2 h under a nitrogen atmosphere. The yellow precipitate formed was collected and washed with cold MeOH and hexane and dried to give **4a** (230 mg, 93%). IR(Nujol): ν(C≡C) 2042 cm^{-1}. ^{1}H NMR ($CDCl_3$, 200 MHz): δ 4.49 (s, 5H, Cp); 8.76–7.06 (m, 39H, Ph, $C_{14}H_9$). $^{31}P\{^1H\}$ NMR ($CDCl_3$, 81 MHz): δ 51.24 (s, PPh_3). $^{13}C\{^1H\}$ NMR ($CDCl_3$, 100 MHz): δ 85.8 (Cp); 112.7 (C_β); 131.7

Table 9
Selected IR vibrational frequencies (as wavenumbers), together with major electronic excitations for $[\mathbf{4b}]^{n+}$ and $[\mathbf{4\text{-}H}]^{n+}$ determined by TD DFT methods using B3LYP/3-21G*, with selected experimental data for comparison

	Expt **4b**	Calc **4b**	IR intensity/oscillator strength	Calc **4-H**	IR intensity/oscillator strength
Vibrational frequencies (IR)/cm^{-1}					
$n = 0$					
C≡C	2041(s)	2044	723	2081	385
Ring	1561(vw)	1575	27	1577	18
$n = 1$					
C≡C	1925(s)	1934	81	1994	628
Ring	1590(w)	1563	12	1551	42
Electronic transitions/cm^{-1} (Molar absorption coefficient/M^{-1} cm^{-1} or calculated oscillator strength, <1)					
$n = 0$					
HOMO → LUMO	20 600(11 600)	21 100(21 100)	0.2147	23 310(23 300)	0.2817
$n = 1$					
β-[HOSO − 1] → β-LUSO	7800(600)	6500(6500)	0.0035	9120(9100)	0.0021
β-[HOSO] → β-LUSO α-HOSO → α-LUSO	10 100(1900)	9710(9700)	0.1163	11 390(11 400)	0.1248
β-[HOSO − 4] → β-LUSO	15 200(5900)	15 550(15 500)[a]	0.0525	19 840(19 800)	0.0442
α-HOSO → α-LUSO	17 900(14 000)	16 530(16 500)	0.0998	17 480(17 500)	0.2714

[a] β-[*HOSO − 3*] → β-*LUSO*

(t, $J_{CP} = 25$ Hz, C_α); 120.3, 123.8 (CH), 124.9 (CH), 126.0, 128.1 (CH), 129.2 (CH), 132.0 (CH), 132.6 (C1–C14); 127.4 (dd, $J_{CP/CCP} \sim 5$ Hz, C_m); 128.6 (C_p); 133.9 (dd, $J_{CP/CCP} \sim 5$ Hz, C_o); 139.0 (dd, $^1J_{CP}/^4J_{CP} \sim 11$ Hz, C_i). ES(+)-MS (*m*/*z*): 892, [M^+]. High resolution: calculated for $RuP_2C_{57}H_{45}$ $[M + H]^+$ 893.20345; found 893.20428.

8.5. Complex *1b*

^{13}C NMR ($CDCl_3$, 100 MHz) for **1b**: δ 10.0 (Me); 92.5 (Cp); 109.6 (C_β); 128.8 (t, $J_{CP} = 25$ Hz, C_α); 122.4 (C4), 127.4 (C3); 130.2 (C2); 131.3 (C1); 127.1, 127.4 (dd, $^3J_{CP}/^6J_{CP} \sim 5$ Hz, $C_{m,m'}$); 128.8, 128.8 ($C_{p,p'}$); 133.2, 133.7 (dd, $^2J_{CP}/^5J_{CP} \sim 5$ Hz, $C_{o,o'}$); 136.9, 138.9 (m, $C_{i,i'}$).

8.6. Preparation of [*Ru*(C≡*CC*$_6$*H*$_4$*Me-4*)(*dppe*)*Cp**] (*2b*)

A suspension of [RuCl(dppe)Cp*] (100 mg, 0.15 mmol), HC≡CC_6H_4Me (35 mg, 0.30 mmol) and NH_4PF_6 (50 mg, 0.3 mmol) in methanol (15 mL) was heated at reflux for 1 h under a nitrogen atmosphere to form a bright red solution, 2–3 drops of NaOMe were added to form yellow precipitate which was collected by filtration, washed with cold MeOH followed by hexane, and air-dried to afford **2b** as a yellow solid (60 mg, 54%). IR(Nujol): ν(C≡C) 2078 cm^{-1}. ^1H NMR ($CDCl_3$, 400 MHz): δ 1.54 (s, 15H, Cp*), 2.21 (s, 3H, Me), 2.04 (2 × dd, 2H, $J_{HP} = J_{HH} = 6$ Hz, dppe), 2.68 (2 × dd, 2H, $J_{HP} = J_{HH} = 6$ Hz, dppe); 6.83 (d, $J_{HH} = 8$ Hz, 2H, C_6H_4); 6.85 (d, $J_{HH} = 7.6$ Hz, 2H, C_6H_4); 7.17–7.79 (m, Ar 20H). $^{31}P\{^1H\}$ NMR ($CDCl_3$, 162 MHz): δ 81.1 (s, dppe). $^{13}C\{^1H\}$ NMR ($CDCl_3$, 100 MHz): δ 10.0 (Me at Cp); 21.1 (Me); 29.5 (dd, $J_{CP/CCP} \sim 23$ Hz, CH_2); 92.5 (Cp); 109.2 (C_β); 126.4 (t, $J_{CP} = 25$ Hz, C_α); 128.2 (CH); 128.5; 130.0 (CH); 131.9 (C1–C4); 127.4, 127.2 (dds, $J_{CP/CCP} \sim 5$ Hz, $C_{m,m'}$); 128.8 ($C_{p,p'}$); 133.8, 133.2 (dds, $J_{CP/CCP} \sim 5$ Hz, $C_{o,o'}$); 137.1, 139.0 (m, $C_{i,i'}$). ES(+)-MS (*m*/*z*): 751, $[M + H]^+$. High resolution: calculated for $RuP_2C_{45}H_{47}$ $[M + H]^+$ 751.21910; found 751.21305.

8.7. Preparation of [*Ru*(C≡*CC*$_{10}$*H*$_7$)(*dppe*)*Cp**] (*3b*)

A solution of [RuCl(dppe)Cp*] (150 mg, 0.22 mmol), HC≡$CC_{10}H_7$ (39 mg, 0.22 mmol) and ammonium hexafluorophosphate (37 mg, 0.22 mmol) in stirring MeOH (10 mL) were heated at reflux for 20 min to form a bright red solution, 2–3 drops of DBU were added to form yellow precipitate which was collected by filtration, washed with cold MeOH (3 mL), and air-dried to afford **3b** as a yellow solid (97 mg, 55%). IR (Nujol): ν(C≡C) 2055 cm^{-1}. ^1H NMR ($CDCl_3$, 400 MHz): δ 1.60 (s, 15H, Cp*); 2.11 (2 × dd, 2H, $J_{HP} = J_{HH} = 6$ Hz, dppe), 2.78 (2 × dd, 2H, $J_{HP} = J_{HH} = 6$ Hz, dppe); 6.75–7.78 (m, 27H, Ar). $^{31}P\{^1H\}$ NMR ($CDCl_3$, 81 MHz): δ 82.5 (s, dppe). $^{13}C\{^1H\}$ NMR ($CDCl_3$, 100 MHz): δ 10.2 (Me), 29.4 (dd, $J_{CP/CCP} \sim 23$ Hz, CH_2); 92.8 (Cp); 108.4 (C_β); 135.1 (t, $J_{CP} = 25$ Hz, C_α); 122.2 (CH), 125.0 (CH), 125.5 (CH), 127.4, 127.6 (CH), 128.1 (CH), 128.4, 133.5 (CH), 134.3 (C1–C10); 127.4, 127.5 (dd, $J_{CP/CCP} \sim 5$ Hz, $C_{m,m'}$); 128.8, 128.9 ($C_{p,p'}$); 133.3, 133.8 (dd, $J_{CP/CCP} \sim 5$ Hz, $C_{o,o'}$);137.1, 139.0 ($C_{i,i'}$). ES(+)-MS (*m*/*z*): 787, $[M + H]^+$. High resolution: calculated for $RuP_2C_{48}H_{47}$ $[M + H]^+$ 787.21910; found 787.22099.

8.8. Preparation of [*Ru*(C≡*CC*$_{14}$*H*$_9$)(*dppe*)*Cp**] (*4b*)

A suspension of [RuCl(dppe)Cp*] (100 mg, 0.15 mmol), $Me_3SiC{\equiv}CC_{14}H_9$ (45 mg, 0.16 mmol), and KF (25 mg,

0.43 mmol) in methanol (15 mL) was heated at reflux for 2 h under a nitrogen atmosphere. The yellow precipitate formed was collected and washed with MeOH and hexane and dried to give **4b** (91 mg, 73%). IR(Nujol): ν(C≡C) 2039 cm^{-1}. ^1H NMR($CDCl_3$, 400 MHz): δ 1.70 (s, 15H, Cp^*); 2.17 (2 × dd, 2H, $J_{HP} = J_{HH} = 6$ Hz, dppe), 2.96 (2 × dd, 2H, $J_{HP} = J_{HH} = 6$ Hz, dppe); 6.86–7.95 (m, 29H, Ph). $^{31}P\{^1H\}$ NMR ($CDCl_3$, 162 MHz) 81.4 (s, dppe). $^{13}C\{^1H\}$ NMR ($CDCl_3$, 100 MHz): δ 10.4 (Me), 29.5 (dd, $J_{CP/CCP} \sim 23$ Hz, CH_2), 93.1 (Cp), 108.5 (C_β); 144.6 (t, $J_{CP} = 25$, C_α); 119.7 (CH), 123.1 (CH), 124.7 (CH), 126.4, 127.7 (CH), 129.1 (CH), 131.9 (CH), 132.2 (CH), 134.2, 136.9 (C1–C14); 127.4, 127.5 (dd, $J_{CP/CCP} \sim 5$ Hz, $C_{m,m'}$); 129.0 ($C_{p,p'}$); 133.4, 133.8 (dd, $J_{CP/CCP} \sim 5$ Hz, $C_{o,o'}$); 137.1, 138.7 (m, $C_{i,i'}$). ES(+)-MS (m/z): 836, $[M + H]^+$. High resolution: calculated for $RuP_2C_{52}H_{49}$ $[M + H]^+$ 836.22693; found 836.22820.

8.9. Computations

All *ab initio* computations were carried out with the Gaussian 03 package [41].The model geometries **1-H**, [**1-H**]$^+$, **4-H** and [**4-H**]$^+$ discussed here were optimised using the B3LYP, [42] or PBE1PBE [43] functionals with no symmetry constraints. The basis sets used here were 3-21G* [44] and two mixed basis sets, named here as Gen and Gen2. Gen contains the pseudo-potentials LANL2DZ [45] for the Ru atom and 6-31G* [46] basis set for all other atoms. Gen2 contains the 3-21G* basis set for Ru and 6-311G** for all other atoms. [46] Frequency calculations were carried out on these optimised geometries at the corresponding levels and shown to have no imaginary frequencies. A scaling factor of 0.95 was applied to the calculated ν(C≡C) frequencies [33]. Molecular orbital and TD DFT computations were carried out on these optimised geometries at the appropriate level of theory.

The barriers in the rotations between the phenyl and the $Ru(PH_3)_2Cp$ groups in **1-H** and [**1-H**]$^+$ were estimated by fixing the dihedral angles P1–Ru–C1–C2 (Fig. 2) at 15° intervals at the B3LYP/3-21G* level of theory. The latter level of theory was also used for the optimisation of the actual geometries of **1b**, [**1b**]$^+$, **4b** and [**4b**]$^+$. Frequency calculations (B3LYP/3-21G*) on these geometries revealed no imaginary frequencies. Molecular orbital and TD DFT computations were then carried out on these optimised geometries at the B3LYP/3-21G* level of theory.

Acknowledgements

We thank the EPSRC for financial support (P.J.L.). A Royal Society Joint Project Grant (P.J.L., F.H.) is gratefully acknowledged. R.L.R. held a postgraduate scholarship from the Durham Chemistry Department Doctoral Training Account. W.M.K. gratefully acknowledges funding from the Human Resources Development in Science and Technology Programme, Ministry of Science, Technology and Innovation, Malaysia.

References

[1] R. Nast, Coord. Chem. Rev. 47 (1982) 89.
[2] R. Zeissel, M. Hissler, A. El-Ghayoury, A. Harriman, Coord. Chem. Rev. 178 (1998) 1251.
[3] M.C. Puerta, P. Valerga, Coord. Chem. Rev. 193–5 (1999) 977.
[4] U. Belluco, R. Bertani, R.A. Michelin, M. Mozzon, J. Organomet. Chem. 600 (2000) 37.
[5] N.J. Long, C.K. Williams, Angew. Chem., Int. Ed. 42 (2003) 2586.
[6] T. Ren, Organometallics 24 (2005) 4854.
[7] W.Y. Wong, C.L. Ho, Coord. Chem. Rev. 250 (2006) 2627.
[8] (a) V.W.W. Yam, Acc. Chem. Res. 35 (2002) 555;
(b) V.W.W. Yam, K.M.C. Wong, Top. Curr. Chem. 257 (2005) 1.
[9] (a) M.P. Cifuentes, M.G. Humphrey, J. Organomet. Chem. 689 (2004) 3968;
(b) C.E. Powell, M.G. Humphrey, Coord. Chem. Rev. 248 (2004) 725.
[10] M. Samoc, N. Gauthier, M.P. Cifuentes, F. Paul, C. Lapinte, M.G. Humphrey, Angew. Chem., Int. Ed. 45 (2006) 7376.
[11] K. Costuas, F. Paul, L. Toupet, J.F. Halet, C. Lapinte, Organometallics 23 (2004) 2053.
[12] (a) M.I. Bruce, K. Costuas, T. Davin, B.G. Ellis, J.F. Halet, C. Lapinte, P.J. Low, M.E. Smith, B.W. Skelton, L. Toupet, A.H. White, Organometallics 24 (2005) 3864;
(b) M.I. Bruce, P.J. Low, K. Costuas, J.F. Halet, S.P. Best, G.A. Heath, J. Am. Chem. Soc. 122 (2000) 1949.
[13] F. Paul, B.G. Ellis, M.I. Bruce, L. Toupet, T. Roisnel, K. Costuas, J.-F. Halet, C. Lapinte, Organometallics 25 (2006) 649.
[14] O.F. Koentjoro, R. Rousseau, P.J. Low, Organometallics 20 (2001) 4502.
[15] (a) D.L. Lichtenberger, S.K. Renshaw, Organometallics 12 (1993) 3522;
(b) D.L. Lichtenberger, S.K. Renshaw, R.M. Bullock, J. Am. Chem. Soc. 115 (1993) 3276;
(c) D.L. Lichtenberger, N.E. Gruhn, S.K. Renshaw, J. Mol. Struct. 405 (1997) 79.
[16] F. Paul, L. Toupet, J.Y. Thepot, K. Costuas, J.F. Halet, C. Lapinte, Organometallics 24 (2005) 5464.
[17] M.I. Bruce, Chem. Rev. 91 (1991) 197.
[18] M.I. Bruce, B.C. Hall, B.D. Kelly, P.J. Low, B.W. Skelton, A.H. White, J. Chem. Soc., Dalton Trans. (1999) 3719.
[19] M.I. Bruce, R.C. Wallis, J. Organomet. Chem. 161 (1978) C1.
[20] C. Bitcon, M.W. Whitely, J. Organomet. Chem. 336 (1987) 385.
[21] (a) C.E. Powell, M.P. Cifuentes, A.M. McDonoagh, S.K. Hurst, N.T. Lucas, C.D. Delfs, R. Stranger, M.G. Humphrey, S. Houbrechts, I. Asselberghs, A. Persoons, D.C.R. Hockless, Inorg. Chim. Acta 352 (2003) 9;
(b) S.K. Hurst, N.T. Lucas, M.P. Cifuentes, M.G. Humphrey, M. Samoc, B. Luther-Davies, I. Asselberghs, R. Van Boxel, A. Persoons, J. Organomet. Chem. 633 (2001) 114;
(c) N.T. Lucas, M.P. Cifuentes, L.T. Nguyen, M.G. Humphrey, J. Cluster Sci. 12 (2001) 201;
(d) I.R. Whittall, M.P. Cifuentes, M.G. Humphrey, B. Luther-Davies, M. Samoc, S. Houbrechts, A. Persoons, G.A. Heath, D.C.R. Hockless, J. Organomet. Chem. 549 (1997) 127;
(e) I.R. Whittall, M.G. Humphrey, A. Persoons, S. Houbrechts, Organometallics 15 (1996) 1935;
(f) I.R. Whittall, M.G. Humphrey, D.C.R. Hockless, B.W. Skelton, A.H. White, Organometallics 14 (1995) 3970.
[22] N.J. Long, A.J. Martin, F. Fabrizi de Biani, P. Zanello, J. Chem. Soc., Dalton Trans. (1998) 2017.
[23] (a) I.-Y. Wu, J.T. Lin, C.-S. Li, C. Tsai, Y.S. Wen, C.-C. Hsu, F.-F. Yeh, S. Liou, Organometallics 17 (1998) 2188;
(b) I.-Y. Wu, J.T. Lin, J. Luo, S.-S. Sun, C.-S. Li, K.L. Lin, C. Tsai, C.-C. Hsu, J.-L. Lin, Organometallics 16 (1997) 2038.
[24] (a) R.L. Cordiner, D. Albesa-Jove, R.L. Roberts, J.D. Farmer, H. Puschmann, D. Corcoran, A.E. Goeta, J.A.K. Howard, P.J. Low, J. Organomet. Chem. 690 (2005) 4908;

(b) M.I. Bruce, B.C. Hall, P.J. Low, B.W. Skelton, A.H. White, J. Organomet. Chem. 592 (1999) 74.
[25] (a) C.J. McAdam, A.R. Manning, B.H. Robinson, J. Simpson, Inorg. Chim. Acta 358 (2005) 1673;
(b) A. Mishra, D.S. Pandey, K. Mishra, U.C. Agarwala, Ind. J. Chem. A 29A (1990) 251.
[26] J.A. Shaw-Taberlet, S. Sinbandhit, T. Roisnel, J.-R. Hamon, C. Lapinte, Organometallics 25 (2006) 5311.
[27] J.E. McGrady, T. Lovell, R. Stranger, M.G. Humphrey, Organometallics 16 (1997) 4004.
[28] C.D. Delfs, R. Stranger, M.G. Humphrey, A.M. McDonagh, J. Organomet. Chem. 607 (2000) 208.
[29] N.G. Connelly, W.E. Geiger, Chem. Rev. 96 (1996) 877.
[30] M. Krejčík, M. Daněk, F. Hartl, J. Electroanal. Chem. 317 (1991) 179.
[31] J.M. Wisner, T.J. Bartczak, J.A. Ibers, Inorg. Chim. Acta 100 (1985) 115.
[32] M.I. Bruce, M.G. Humphrey, M.R. Snow, E.R.T. Tiekink, J. Organomet. Chem. 314 (1986) 213.
[33] (a) It is known that DFT calculations over estimate the acetylide ν(C≡C) and acetylide ring substituent ν(C=C) frequencies, and a scaling factor of 0.95 has been employed in the data presented in this work. See A.P. Scott, L. Radom, J. Phys. Chem. 100 (1996) 16502;
(b) J.C. Roder, F. Meyer, I. Hyla-Kryspin, R.F. Winter, E. Kaifer, Chem. Eur. J. 9 (2003) 2636.
[34] C.E. Powell, M.P. Cifuentes, J.P. Morrall, R. Stranger, M.G. Humphrey, M. Samoc, B. Luther-Davies, G.A. Heath, J. Am. Chem. Soc. 125 (2003) 602.
[35] C.Y. Wong, C.M. Che, M.C.W. Chan, J. Han, K.H. Leung, D.L. Phillips, K.Y. Wong, N.Y. Zhu, J. Am. Chem. Soc. 127 (2005) 13997.
[36] M.I. Bruce, C. Hameister, A.G. Swincer, R.C. Wallis, Inorg. Synth. 28 (1990) 270.
[37] M.I. Bruce, B.G. Ellis, P.J. Low, B.W. Skelton, A.H. White, Organometallics 22 (2003) 3184.
[38] M.I. Bruce, C. Hameister, A.G. Swincer, R.C. Wallis, Inorg. Synth. 21 (1982) 78.
[39] (a) H. Matsuzaka, Y. Sato, H. Okimura, T. Ishii, M. Yamashita, S. Kitagawa, M. Kondo, M. Shiro, M. Yamasaki, Chem. Lett. (1999) 865;
(b) H. Matsuzaka, H. Okimura, Y. Sato, T. Ishii, M. Yamashita, M. Kondo, S. Kitagawa, M. Shiro, M. Yamasaki, J. Organomet. Chem. 625 (2001) 133.
[40] M.E. Wright, D.A. Schorzman, Macromolecules 34 (2001) 4768.
[41] M.J. Frisch, G.W. Trucks, H.B. Schlegel, G.E. Scuseria, M.A. Robb, J.R. Cheeseman, J.A. Montgomery Jr., T. Vreven, K.N. Kudin, J.C. Burant, J.M. Millam, S.S. Iyengar, J. Tomasi, V. Barone, B. Mennucci, M. Cossi, G. Scalmani, N. Rega, G.A. Petersson, H. Nakatsuji, M. Hada, M. Ehara, K. Toyota, R. Fukuda, J. Hasegawa, M. Ishida, T. Nakajima, Y. Honda, O. Kitao, H. Nakai, M. Klene, X. Li, J.E. Knox, H.P. Hratchian, J.B. Cross, C. Adamo, J. Jaramillo, R. Gomperts, R.E. Stratmann, O. Yazyev, A.J. Austin, R. Cammi, C. Pomelli, J.W. Ochterski, P.Y. Ayala, K. Morokuma, G.A. Voth, P. Salvador, J.J. Dannenberg, V.G. Zakrzewski, S. Dapprich, A.D. Daniels, M.C. Strain, O. Farkas, D.K. Malick, A.D. Rabuck, K. Raghavachari, J.B. Foresman, J.V. Ortiz, Q. Cui, A.G. Baboul, S. Clifford, J. Cioslowski, B.B. Stefanov, G. Liu, A. Liashenko, P. Piskorz, I. Komaromi, R.L. Martin, D.J. Fox, T. Keith, M.A. Al-Laham, C.Y. Peng, A. Nanayakkara, M. Challacombe, P.M.W. Gill, B. Johnson, W. Chen, M.W. Wong, C. Gonzalez, J.A. Pople, GAUSSIAN 03, Revision C.02, Gaussian Inc., Wallingford, CT, 2004.
[42] (a) A.D. Becke, J. Chem. Phys. 98 (1993) 648;
(b) C. Lee, W. Yang, R.G. Parr, Phys. Rev. B 37 (1988) 785;
(c) A.D. Becke, Phys. Rev. A 38 (1988) 3098;
(d) J.P. Perdew, Phys. Rev. B 33 (1986) 8822.
[43] J.P. Perdew, K. Burke, M. Ernzerhof, Phys. Rev. Lett. 77 (1996) 3865.
[44] (a) G.A. Petersson, M.A. Al-Laham, J. Chem. Phys. 94 (1991) 6081;
(b) G.A. Petersson, A. Bennett, T.G. Tensfeldt, M.A. Al-Laham, W.A. Shirley, J. Mantzaris, J. Chem. Phys. 89 (1988) 2193.
[45] (a) T.H. Dunning Jr., P.J. Hay, in: H.F. SchaeferIII (Ed.), Modern Theoretical Chemistry, vol. 3, Plenum, New York, 1976, pp. 1–28;
(b) P.J. Hay, W.R. Wadt, J. Chem. Phys. 82 (1985) 270;
(c) W.R. Wadt, P.J. Hay, J. Chem. Phys. 82 (1985) 284;
(d) P.J. Hay, W.R. Wadt, J. Chem. Phys. 82 (1985) 299.
[46] (a) G.A. Petersson, M.A. Al-Laham, J. Chem. Phys. 94 (1991) 6081;
(b) G.A. Petersson, A. Bennett, T.G. Tensfeldt, M.A. Al-Laham, W.A. Shirley, J. Mantzaris, J. Chem. Phys. 89 (1988) 2193.